Monthly Notices
of the
ROYAL ASTRONOMICAL SOCIETY

MNRAS **460,** 1555–1566 (2016) doi:10.1093/mnras/stw1118
Advance Access publication 2016 May 12

Wolf–Rayet stars in M81: detection and characterization using GTC/OSIRIS spectra and *HST*/ACS images

V. M. A. Gómez-González,★ Y. D. Mayya★ and D. Rosa-González★

Instituto Nacional de Astrofísica, Óptica y Electrónica, Luis Enrique Erro 1, Tonantzintla 72840, Puebla, Mexico

Accepted 2016 May 10. Received 2016 May 9; in original form 2015 December 24

ABSTRACT

We here report the properties of Wolf–Rayet (W–R) stars in 14 locations in the nearby spiral galaxy M81. These locations were found serendipitously while analysing the slit spectra of a sample of ∼150 star-forming complexes, taken using the long-slit and multiobject spectroscopic modes of the OSIRIS instrument at the 10.4-m Gran Telescopio Canarias. Colours and magnitudes of the identified point sources in the *Hubble Space Telescope* images compare well with those of individual W–R stars in the Milky Way. Using templates of individual W–R stars, we infer that the objects responsible for the observed W–R features are single stars in 12 locations, comprising of three WNLs, three WNEs, two WCEs and four transitional WN/C types. In diagrams involving bump luminosities and the width of the bumps, the W–R stars of the same sub-class group together, with the transitional stars occupying locations intermediate between the WNE and WCE groups, as expected from the evolutionary models. However, the observed number of 4 transitional stars out of our sample of 14 is statistically high as compared to the 4 per cent expected in stellar evolutionary models.

Key words: stars: Wolf–Rayet – galaxies: individual: M81 – galaxies: star clusters: general.

1 INTRODUCTION

The mere detection of Wolf–Rayet (W–R) stars reveals recent burst of high-mass star formation in galaxies (Schaerer & Vacca 1998). This is because the W–R stars are the short-lived descendants of massive O-type stars (>25 $M_\odot$ at solar metallicity ($Z_\odot$); Conti 1976; Meynet & Maeder 2003, 2005), spending ∼10 per cent of their $\lesssim$5 Myr lifetime as a W–R star. During the W–R phase, the most massive of them pass through nitrogen-rich (WN), and then carbon-rich (WC) sequence and finally explode as a supernova. W–R stars are characterized by heavy mass loss (∼10^{-5}–10^{-4} $M_\odot$ yr^{-1}; Crowther 2007, and references therein) through powerful stellar winds. The lost mass not only deposits energy, but also freshly processed elements to the interstellar medium (ISM), which makes these stars important in the study of the dynamics as well as the chemical evolution of galaxies (Hillier 2000). W–R stars are also considered as progenitors of long-period γ-ray bursts (Woosley & Bloom 2006). Alternatively, W–R stars can also be formed in relatively lower mass stars when they are in a binary system (e.g. Vanbeveren 2011).

In the optical range of the spectrum, the presence of W–R stars can be easily inferred by their unique, strong, broad emission features, better known in the literature as W–R bumps. These bumps are mostly composed of blended broad emission lines of He, N and C in various ionization states. The so-called blue bump around 4600–4700 Å is the characteristic feature of all W–R stars. Nitrogen sequence (WN subtype) stars contain essentially only the 'blue bump' composed of He (He II λ4686) and N (N III λλ4634/42) lines, both being products of H-burning via the CNO cycle. On the other hand, the 'red bump' around 5750–5850 Å occurs essentially only in stars of the carbon (WC) and oxygen sequence (WO). These stars have strong emission lines of He (He II λ4686) and C (C III λ4650/C IV λ4658 and C IV λλ5802/12), with WO stars in addition having lines of O (O VI λλ3811/34), all these being the products of He-burning via the triple-α process (Crowther 2007). Hydrogen lines are normally absent in W–R stars, but there is also a subset of W–R stars that show hydrogen lines in emission or absorption. These stars are H-burning and share some similarities with Of-type stars (Crowther, Hillier & Smith 1995; Crowther 2007).

Most of our knowledge on W–R stars is based on the study of individual stars in the Milky Way (MW) (van der Hucht 2001, see also the web page by Paul Crowther[1] for an up-to-date catalogue), the Small Magellanic Cloud (SMC: Massey 2003) and Large Magellanic Cloud (LMC: Breysacher, Azzopardi & Testor 1999). Recent advances in observational techniques, especially the wide-field narrow-band imaging capabilities on large telescopes accompanied by multiobject spectroscopy (MOS), have allowed studies of W–R

★E-mail: mau.gglez@gmail.com (VMAG-G); ydm@inaoep.mx (YDM); danrosa@inaoep.mx (DR-G)

[1] http://www.pacrowther.staff.shef.ac.uk/WRcat/

stars in nearby galaxies such as M33 (Neugent & Massey 2011), M31 (Neugent et al. 2012), M83 (Hadfield et al. 2005), NGC 7793 (Bibby & Crowther 2010) and M101 (Shara et al. 2013). Also large numbers of W–R stars have been detected in the integrated spectra of regions in star-forming galaxies (e.g. Terlevich et al. 1996; Hadfield et al. 2005; Kehrig et al. 2013; Miralles-Caballero et al. 2014). The giant spiral M81 has not yet been a target for a systematic search for W–R stars in spite of it being at only a distance of 3.63 Mpc ($m - M = 27.8$; Freedman et al. 1994). Until now there is report of only 6 W–R detections in the entire galaxy (Patterson et al. 2012). We here report the properties of 14 W–R detections, 13 of them new detections, all discovered serendipitously in slit spectra passing through star-forming regions in the disc of M81 using the long-slit and MOS configurations of the OSIRIS[2] instrument at the 10.4-m Gran Telescopio Canarias (GTC).[3] The MOS data presented here are among the first observations using this mode at the GTC.

This paper is structured as follows: the strategy used for the search of W–R stars, as well as the data used in this work and their reduction, are described in Section 2. In Section 3 we present the technique used to classify the W–R stars. Relations between the obtained parameters for different W–R subtypes in M81 are discussed in the context of currently accepted models for the formation of different W–R subtypes in Section 4. Results are summarized in Section 5.

2 W–R SAMPLE AND OBSERVATIONAL DATA

2.1 The sample and spectroscopic observations

The sample of W–R stars is drawn from an observational programme to study spectroscopically the cluster populations in M81 using the OSIRIS instrument at the GTC (see e.g. Mayya et al. 2013a,b, 2014; Arellano-Córdova et al. 2016). The targets for this programme were mainly Compact Stellar Clusters (CSCs) associated with recent star-forming sites catalogued by Santiago-Cortés, Mayya & Rosa-González (2010). The entire data set used for this work consists of three different observing runs, the first two using long-slits and the last one using MOS. These observations were sensitive enough to register continuum and/or emission-line spectra of individual massive stars at the distance of M81. This realization led us to carry out a comprehensive search for the W–R bumps not only at the position of the targeted clusters, but all along our reduced 2-D spectral images of the long-slit. This search resulted in the discovery of five objects along the nine long-slits from the two runs in 2010 and 2012.

After observing an association of W–R detections with bubble morphologies, the slitlets for two of the three MOS pointings during the 2014 run was chosen to pass through CSCs surrounded by Hα bubbles/shells as seen in the *F606W* image of *HST*. Search for W–R features in the resulting spectra led to the discovery of nine additional W–R objects. Thus, we have a combined sample of 14 objects with W–R features. Five of these objects coincided with the central position of CSCs in the sample of Santiago-Cortés et al. (2010), with the remaining objects appearing in the peripheral parts of the compact clusters or in open clusters. Fig. 1 shows the positions of all the long-slits and the MOS fields on a *GALEX*[4] image and the 14 locations where the spectra registered W–R features. A log of all observations is given in Table 1.

Both the long-slit and MOS observations were carried out using R1000B grism with a slit-width of ∼1.2 arcsec, covering a spectral range from ∼3700 to 7500 Å, at a spectral resolution of ∼7 Å. The observations were carried out with a CCD binning of 2 × 2 resulting in a spatial scale of 0.254 arcsec pixel^{-1} (horizontal axis) and spectral sampling of ∼2 Å pixel^{-1} (vertical axis). The long-slits were 7.4 arcmin long, whereas each MOS observation included ∼30–40 slitlets of varying lengths over a field of view of ∼7.4 arcmin× 2 arcmin. These slitlets included object-free regions for subtraction of the sky spectra, and additional ∼5–6 stars as fiducial points for astrometry.

All the observations were carried out in the service mode, with the total observing time split into blocks of ∼60–90 min. Each block corresponded to a particular long-slit position or a MOS pointing, and consisted of three exposures of equal integration time, to facilitate later removal of cosmic ray hits. The observing runs involved a total of 12 observing blocks. Data for each block contained ancillary files that included standard stars, bias, flat-field and arc lamps. The sky was stable during all the observations where W–R bumps were detected.

2.2 Spectroscopic reductions

Reduction of spectroscopic data was carried out using the package *GTCMOS*, a tailor-made IRAF-based pipeline developed by one of us (YDM)[5] for the reduction of the GTC/MOS and long-slit spectra. The pipeline uses the standard spectroscopic tasks available in IRAF[6] to carry out the reductions. As this is the first paper that uses this pipeline, we will explain briefly the reduction procedure below.

The OSIRIS instrument registers the spectra on two CCDs, with the dispersion axis running vertically on a single CCD. As a first step of the reduction procedure, the pipeline creates a single spectral image of 2110 × 2051 pixels, by tiling the two individual CCD images, using an IRAF script provided by the OSIRIS team. The geometrical distortions of the images were corrected in this step. A master bias image is created for each observing block by combining all tiled bias frames using median algorithm, which is then subtracted from all images of that block. The multiple images of the target objects (three in our case) within a single observing block were then combined using the median algorithm, in the process cleaning the image of cosmic ray events. Each observing block contained multiple exposures of arc-lamp spectra of Ne, Hg and Ar for both long-slit and MOS observations. The arc spectra in the two CCDs were tiled into a single spectral image. The tiled images of all available arc spectra were summed to get a single arc image, which is then used for wavelength calibration. GTCMOS tasks *omstart*, *omcombine* and *omidentify* accomplish the above described functions.

[2] OSIRIS (Optical System for Imaging and low-Intermediate-Resolution Integrated Spectroscopy; http://www.gtc.iac.es/instruments/osiris/osiris.php) is an imager and spectrograph for the optical wavelength range, located in the Nasmyth-B focus of GTC.

[3] Gran Telescopio Canarias is a Spanish initiative with the participation of Mexico and the US University of Florida, and is installed at the Roque de los Muchachos in the island of La Palma. This work is based on the proposals GTC-10A, GTC-12B and GTC-14A, all using Mexican share of the GTC time.

[4] http://galex.stsci.edu/GR6/

[5] http://www.inaoep.mx/∼ydm/gtcmos/gtcmos.html

[6] IRAF is distributed by the National Optical Astronomy Observatory, which is operated by the Association of Universities for Research in Astronomy (AURA) under cooperative agreement with the National Science Foundation.

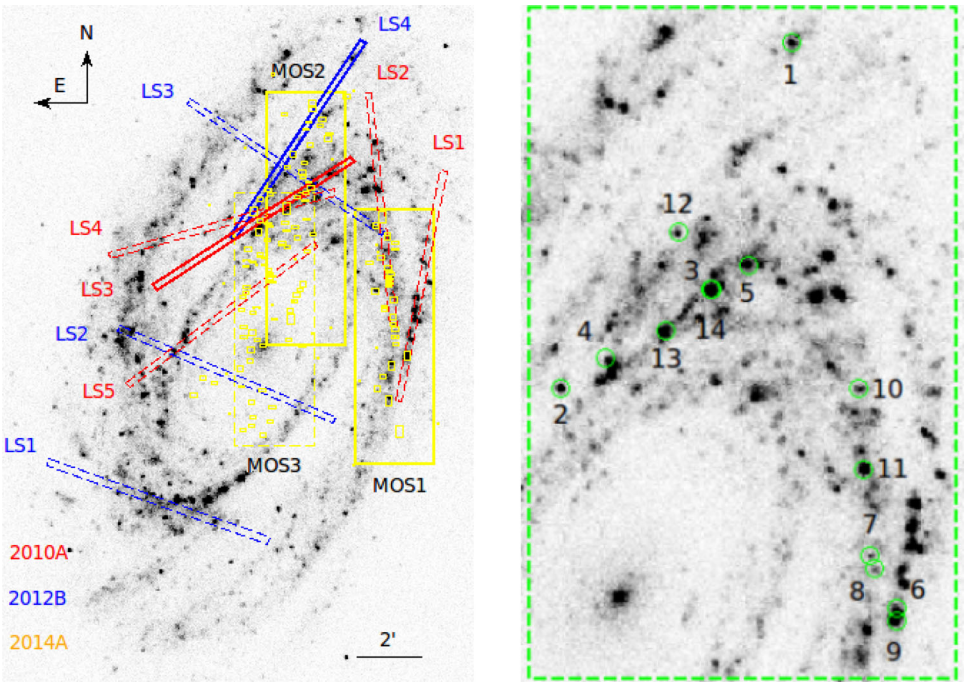

Figure 1. (Left) *GALEX* near-UV image of M81 showing the location of long-slits and MOS for the three different observing runs with GTC/OSIRIS. The long-slits are shown in red for 2010A and blue for 2012B, and the three different MOS fields are shown by yellow rectangles, each enclosing the individual slitlet positions. For the sake of clarity, slit-widths are amplified by a factor of 10 from the original width of ∼1.2 arcsec. The slits or MOS fields where the W–Rs are detected are shown by solid lines (2010-LS3; 2012B-LS4, 2014A-MOS1 and 2014A-MOS2). The orientation and a scale of 2 arcmin are also shown. (Right) The spatial locations of the 14 detected W–R stars are indicated by green circles with their respective identification numbers.

Table 1. Log of the long-slit and MOS spectroscopic observations with GTC/OSIRIS in M81.

Run/mode (1)	PI (2)	Date (3)	PA (4)	SW (5)	Exp. time (6)	AM (7)	Seeing (8)	Night (9)	Std (10)	W–R# (11)
2010A-LS1	D. Rosa-González	2010-04-05	169.22	1.00	3 × 900	1.31	0.80	G	Feige34	–
2010A-LS2	D. Rosa-González	2010-04-05	6.24	1.00	3 × 900	1.33	0.80	G	Feige34	–
2010A-LS3	D. Rosa-González	2010-04-05	123.23	1.00	3 × 900	1.41	0.80	G	Feige34	2–5
2010A-LS4	D. Rosa-González	2010-04-05	105.20	1.00	3 × 900	1.56	0.80	G	Feige34	–
2010A-LS5	D. Rosa-González	2010-04-06	127.20	1.00	3 × 900	1.43	0.80	G	Feige34	–
2012B-LS1	Y. D. Mayya	2013-01-12	250.50	1.23	3 × 1500	1.31	0.79	D	Feige34	–
2012B-LS2	Y. D. Mayya	2013-01-12	247.00	1.23	3 × 1500	1.40	0.97	D	Feige34	–
2012B-LS3	Y. D. Mayya	2013-01-12	56.10	1.23	3 × 1500	1.32	1.20	D	Feige34	–
2012B-LS4	Y. D. Mayya	2013-01-13	146.58	1.23	3 × 1500	1.35	0.95	D	Feige34	1
2014A-MOS1	Y. D. Mayya	2014-04-03	0.00	1.20	3 × 1308	1.31	0.90	D	Ross 640	6–11
2014A-MOS2	Y. D. Mayya	2014-03-23	0.00	1.20	3 × 1308	1.35	1.00	D	Ross 640	12–14
2014A-MOS3	Y. D. Mayya	2014-04-03	0.00	1.20	3 × 1308	1.34	0.80	D	Ross 640	–

Note. Brief explanation of columns: (1) observing run (YYYYx-MOD#, where YYYY is the year, x=Semester (A or B), MOD=observing mode (LS=long-slit or MOS) and # = observing block number; (2) principal investigator; (3) observational date (year-month-date); (4) position angle (°) of the slit as measured on the astrometrized image; (5) slit-width (arcsec); (6) exposure time (number of exposures × integration time in seconds); (7) mean airmass of the three integrations; (8) Seeing (arcsec); (9) night (G = grey or D = dark), clear skies (cirrus reported only for 2010A-LS5); (10) standard star name; (11) detected W–R ID number.

The slit image in the spatial direction has significant curvature. The task *omidentify* straightens this curvature by analysing one arc-lamp spectrum for every section of 20 pixels in the long-slit mode, or at the centre of every slitlet in the MOS mode. Line identification and centring were carried out by an automatic routine that uses ∼10 bright unblended lines in the useful spectral range for each grism. Independent dispersion solutions are obtained for every MOS slitlet (or for image section of 20 pixels in the long-slit mode) with the IRAF task *identify* using a *spline3* function of order 2. Solutions that resulted in an rms error of >0.5 Å were improved by manually examining the fitted residuals. Final rms errors in all cases remained better than 0.5 Å, with the majority having rms errors <0.2 Å. The best-fitting solution for each image section is used to create a wavelength calibrated 2-D image, where the spectral axis was linearly re-sampled to have a common dispersion of 2.1 Å pixel^{-1}, the mean resolution for the grism R1000B. Tilts/curvatures within a MOS slitlet or in a 20-pixel section of a long-slit are corrected by linearly shifting the dispersion-corrected spectra so as to force the centroid of the [O I]λ5577 sky line in every spectrum in that section to its rest wavelength. The procedure followed by the pipeline ensured that the skylines are perfectly horizontal in the 2-D spectral image for both long-slit and

Table 2. Sample of W–R stars in M81.

ID (1)	R.A. (2)	DEC (3)	V (4)	$B-V$ (5)	$B-I$ (6)	M_V (7)	Complex (8)	Cluster (9)	D (10)	Size_{neb} (11)	V_{helio} (12)
WR1	148.756 93	69.215 993	21.29	0.54	0.24	−6.51	Munch 18	F04B16353	1.0	100	38
WR2	148.934 58	69.122 063	20.54	−0.14	−0.26	−7.27	R06B06945	R06B06945	0.0	100	50
WR3	148.819 38	69.148 725	19.53	0.06	0.09	−8.27	kauf152	R03B16992	0.0	250	137
WR4	148.899 54	69.130 043	22.64	0.02	−0.66	−5.16	–	–	–	–	58
WR5	148.790 77	69.155 475	23.07	−0.19	−0.41	−4.73	–	R03B08603	1.5	–	191
WR6	148.677 59	69.061 852	21.56	−0.08	−0.21	−6.24	kauf125	R04B15666	5.0	20	9
WR7	148.698 02	69.076 172	20.46	0.18	0.37	−7.34	kauf127	R04B07520	0.0	80	43
WR8	148.694 82	69.072 919	21.45	0.06	0.10	−6.35	–	R04B08657	0.0	80	25
WR9	148.677 36	69.058 316	22.37	0.40	0.20	−5.43	kauf125	–	–	100	−14
WR10	148.705 91	69.121 952	21.90	0.54	0.59	−5.90	kauf135	R02B18517	0.0	80	110
WR11	148.702 68	69.099 903	19.30	0.17	−0.12	−8.50	kauf128	R04B01345	3.0	80	90
WR12	148.844 51	69.164 518	21.78	0.35	0.20	−6.02	–	–	–	100	86
WR13	148.854 11	69.137 450	20.22	0.14	0.20	−7.58	kauf159	R03B25826	3.0	250	104
WR14	148.818 70	69.148 704	22.17	0.19	0.11	−5.63	kauf152	R03B16992	2.0	250	192

Note. Brief explanation of columns: (1) name of the W–R star adopted in this study; (2–3) Right Ascension and declination in the FK5 system on the astrometrized *HST* image, where the M81 nucleus is located at RA=148°.888 89 (9:55:33.333) and Dec=69°.065 333 (+69:03:55.20) (4-6) Apparent magnitude and colours in *F*435*W* (*B*), *F*606*W* (*V*) and *F*814*W* (*I*) bands; (7) absolute magnitude in *F*606*W* band (M_V) using a distance modulus of 27.80 mag, and Galactic extinction $A_V = 0.20$ mag (Schlafly & Finkbeiner 2011); (8) star-forming complex from Pérez-González et al. (2006) embedding the W–R star; (9) compact stellar cluster from Santiago-Cortés et al. (2010) within 100 pc (5.7 arcsec) that is closest to the W–R; (10) distance to the compact stellar cluster in arcsec; (11) size in parsec of the nebulosity around the W–R star as measured on the *F*606*W* image; (12) heliocentric radial velocity in km s^{-1} of the nebular lines in the extracted W–R spectrum.

MOS modes. The GTCMOS task *omreduce* accomplishes these functions.

The basic reduction of the standard star spectra followed a procedure similar to that described above. All independent standard star exposures within an observing block were reduced individually. The spectra were extracted and the IRAF task *standard* was used to obtain the sensitivity tables between the flux and count rate at all available spectral bands of the catalogued standard star. The sensitivity tables for all exposures within an observing block were averaged at every wavelength band and fitted with a spline3 function of order 6 using the IRAF task *sensfunc* to obtain a mean sensitivity function. The extinction curve for the observatory, along with the observed airmass, were used for the purpose of atmospheric extinction correction.

M81 is a large galaxy even for the relatively large field of view of the OSIRIS instrument, which implies that the galaxy disc has contribution even in the designated sky slitlets in the MOS mode or the apparently object-free pixels of the long-slit. We examined the *HST* images at the positions of the slits to search for pixels that are devoid of point sources. Spectra of such sections were used to obtain a sky + disc spectra, which were then subtracted from each object spectrum. In regions with varying disc contribution, care was taken to subtract the disc spectrum spatially closest to the object.

We found that the flat-fields in the blue part of the spectrum do not have the signal-to-noise ratio suitable for the correction of the relative efficiencies of pixels, even when the red part of the spectrum is saturated. Thus, in order to avoid degrading the blue part of the target spectra, we carried out the reductions without applying corrections for flat-fielding and illumination variations along the long-slit, or from one slitlet to another in the MOS mode. The flat-field errors are expected to be less than a percent, whereas the residual error due to the non-correction for illumination variations is estimated to be at the most 2 per cent per cent, as judged by the relative intensities of the skyline along the spatial direction.

2.3 Detection of W–R features and extraction of spectra

We visually examined the wavelength-calibrated and sky-subtracted 2-D spectral image from all the runs for the presence of blue and/or red bumps. This procedure resulted in the identification of 14 regions with W–R features. Continuum is detected at the location of all the 14 W–R features, with the continuum having a higher spatial extent than that of the W–R feature in some cases. Typically the width of the blue bump in the spatial direction was measured to be of the seeing size (4–5 pixels). On the other hand, the nebula as traced by the H β line extended much more in the spatial direction.

We followed a similar procedure for the extraction of 1-D spectrum from our long-slit and MOS 2-D spectral images. The IRAF task *apall* was used for this purpose. We tuned the *apall* parameters so as to maximize the strength of W–R bumps in the extracted 1-D spectrum. This is achieved by centring the extraction window on the peak of the blue bump and the spectra were traced around this pixel. In a few cases (3) that had a weak continuum, we used a bright nearby continuum object as a reference for tracing, whereas in a few others that had a broad continuum, we restricted the trace width to 5 pixels. A residual sky is subtracted by choosing a local sky region interactively.

All extracted spectra are rich in nebular emission lines, originating in an ionized nebula around the W–R stars. Bright nebular lines in these spectra were used to determine the radial velocity for each spectrum, which are given in the last column of Table 2. All spectra were brought to the rest-frame wavelength using these measured velocities. The Doppler-corrected spectra for all the 14 W–R stars are shown in Fig. 2. The blue and red bumps can be easily noticed around 4650 Å and 5810 Å.

It is desirable to have W–R spectra free of nebular lines for an easy identification of all features responsible for W–R stars. Our slits registered nebular spectra from regions surrounding the W–R sources. These spectra are Doppler-corrected using the velocities measured in these spectra, and are scaled using the fluxes of the H β line, before using them for subtracting the nebular contamination

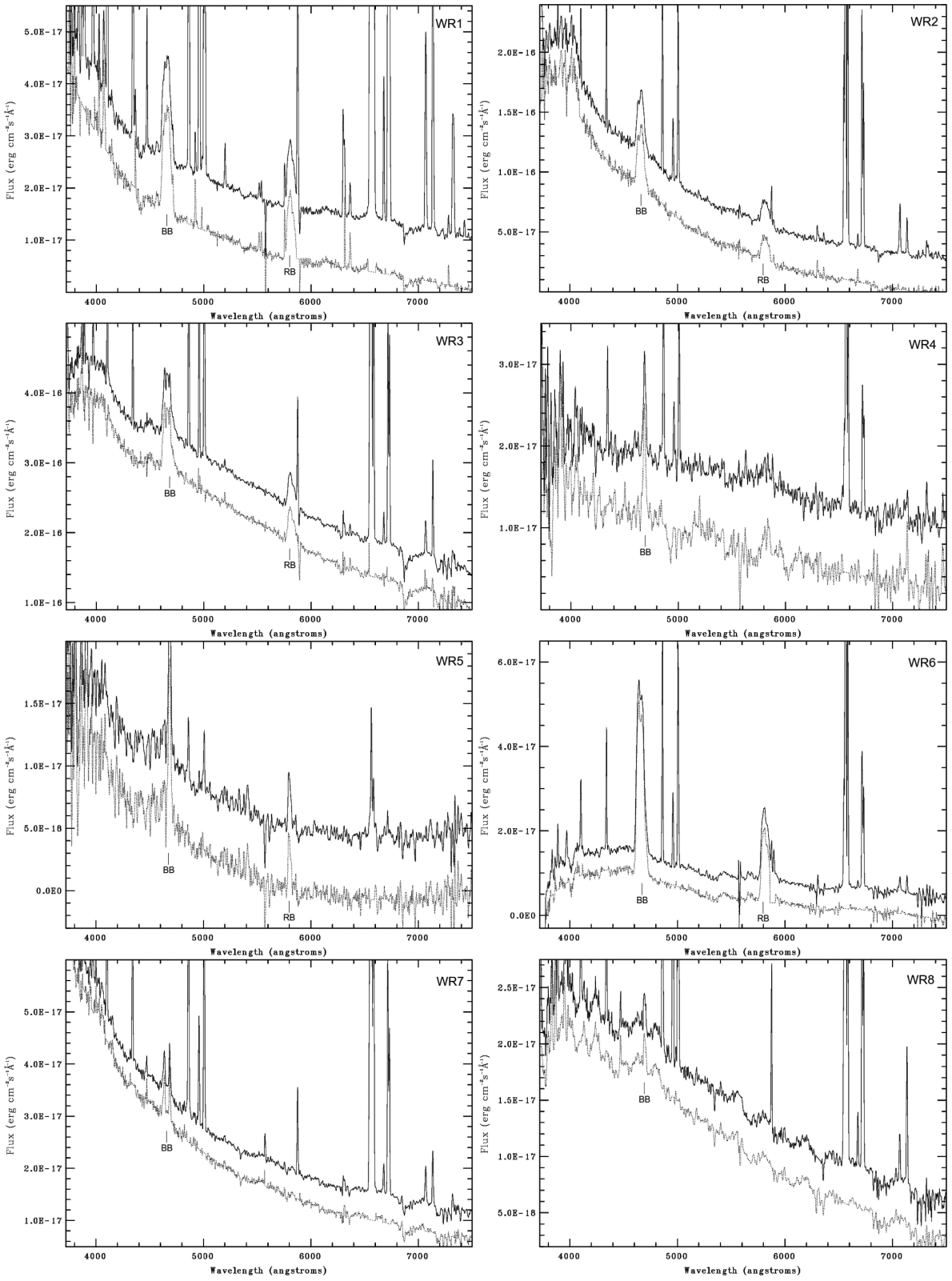

Figure 2. Extracted spectrum of each of the 14 locations containing W–R features (above) is plotted along with the corresponding nebular-free spectrum (below) in each panel. The latter spectra are shifted downwards by appropriate amounts for the sake of clarity. The top right corner of each panel contains the W–R identification. The blue and red bumps, when present, are marked by letters BB and RB, respectively.

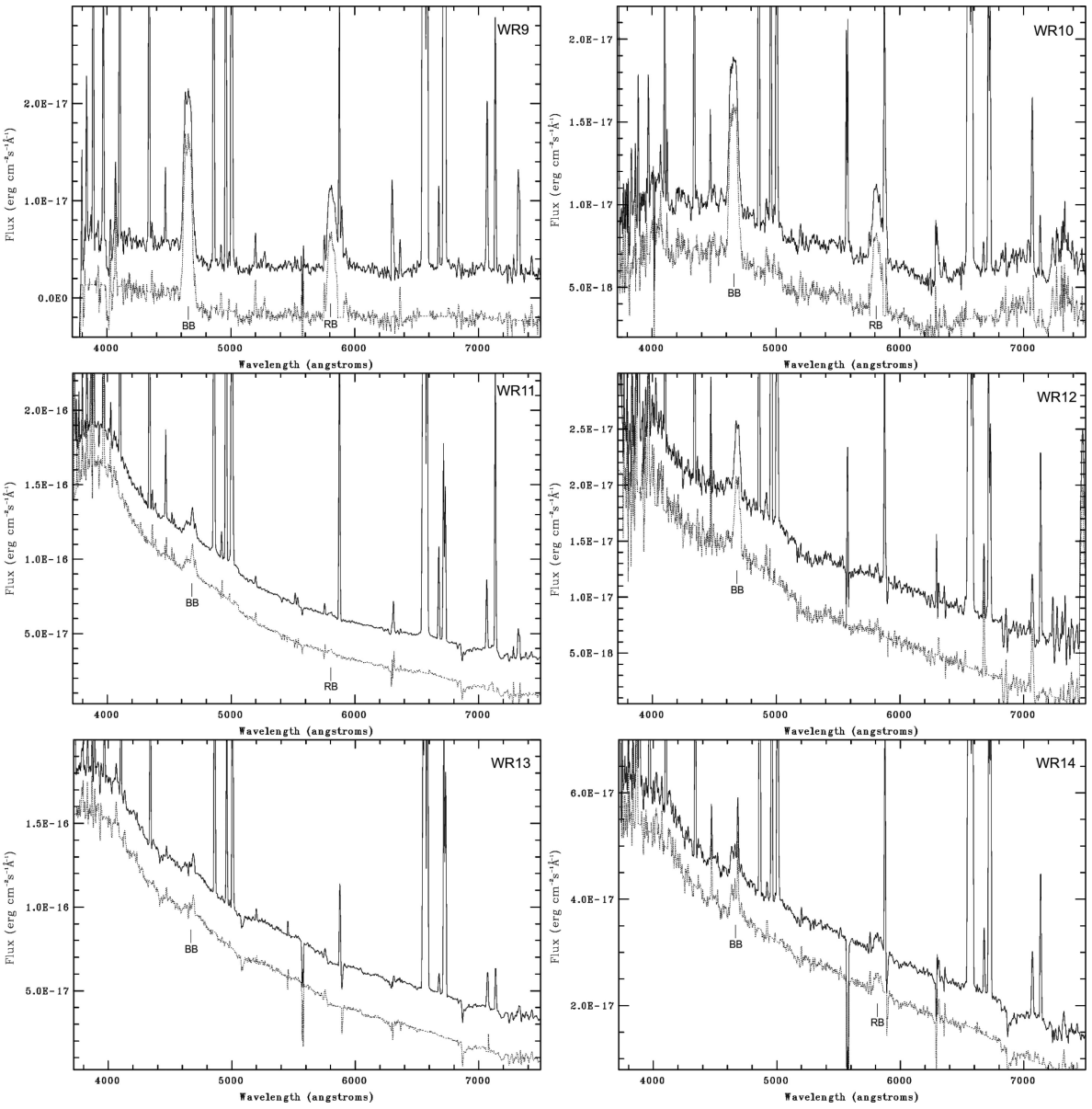

Figure 2 – *continued*

in the W–R spectrum. The residual fluxes of the nebular lines in the resulting pure W–R spectrum are around 20 per cent of the original flux, which limits the detection of any W–R line coincident with a nebular line (e.g. Hα, Hβ, He I λ5876 etc.). In order to avoid any misinterpretation of the residuals, we replaced the part of the spectrum containing a nebular line with continuum fitted to the original W–R spectrum. The adopted technique allows us to easily identify W–R lines that are not coincident with the lines in the surrounding nebula. The resulting nebular-free spectra are plotted below the observed spectra in Fig. 2. Analysis of the W–R features in these spectra will be presented in Section 3.

2.4 Localization of W–R stars using the *HST* images

The physical scale of our slit-width ($\sim$20 pc) is large enough to include more than one star, and hence the W–R features seen in our spectra may not be necessarily originating in single stars. We hence use the 10 times better spatial resolution offered by the *HST*/ACS images in an attempt to identify the object(s) responsible for W–R features. The *HST* data base has images in the *B* (*F*435*W*), *V* (*F*606*W*) and *I* (*F*814*W*) (PI: Andreas Zesas) bands for M81, all using the ACS. The *F*606*W* filter intercepts the Hα line, which allows us to trace the nebular emission, if any, at the *HST* resolution.

The following procedure was adopted for locating the W–Rs on the *HST* images. All the GTC observing blocks contained two acquisition images in the SDSS *r*-band; one of the slit, and the other of the entire field of view of $\sim$60 s and 10 s durations, respectively. We astrometrized the latter image with respect to the *HST* image using $\sim$20 field stars, giving us an astrometric accuracy of $\sim$0.1 arcsec rms. We then superposed the long-slit/MOS slitlets on an RGB colour image formed from the *F*814*W* (*R*), *F*606*W* (*G*) and *F*435*W* (*B*) images. On this image, we searched for the W–R star around the position calculated in the acquisition image within an error box of 0.1 arcsec$\times$ *slit* $-$ *width*. In majority of the cases, the brightest object is the closest to the expected position. Often, this object occupies the centre of the nebula, and the nebular size

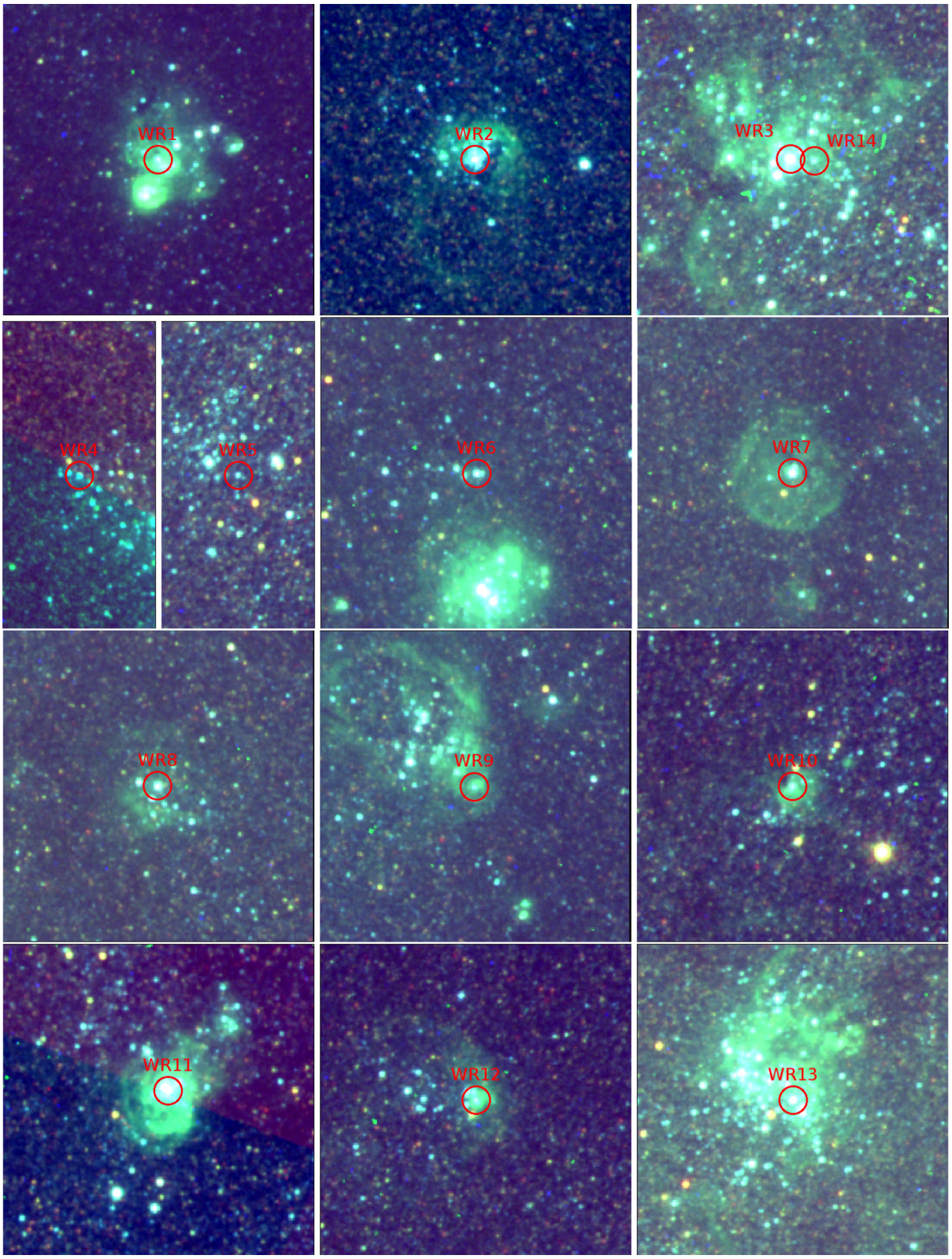

Figure 3. RGB images using the *HST*/ACS *F*814*W* (*R*), *F*606*W* (*G*) and *F*435*W* (*B*) bands showing the large-scale morphology of ionized gas and stars around the W–R star locations. The sections are of physical size 200 × 200 pc in all cases except in WR4 and WR5 where the sizes correspond to 100 × 200 pc. The W–R locations are shown by red circles. The ionized gas is seen as green emission in these images, which is due to the H α line entering the *F*606*W* filter. All images are oriented north at the top and east to the left.

measured using the Hα line in the spectrum is in agreement with that measured on the *F*606*W* image. In three cases, there were 2–3 candidates within the search box. In such cases, we selected the one closest to the expected position and/or the brightest object within the search box. The positions of the identified W–R stars are marked in Fig. 3, where the diameter of the circle corresponds to 1 arcsec, which is the typical slit-width in our observations.

2.5 Large-scale morphology around the W–R stars

We now examine the large-scale environment around the identified W–R locations. For this purpose, we use the RGB images generated using the *HST*/ACS *F*814*W* (*R*), *F*606*W* (*G*) and *F*435*W* (*B*) bands (Fig. 3). In particular, we use the *F*606*W* image which traces the nebular emission (seen as green colour in our RGB images). Large-scale (∼100 pc) ionized gas is seen in all but two cases, with the exceptions being WR4 and WR5. Small-scale (<20 pc) ionized gas is present however even in these two cases as can be inferred from the nebular emission lines in their spectra.

All W–R stars in our sample are part of a star-forming complex, or an open cluster. In column 8 of Table 2 we list the name, when available, of the star-forming complex containing the W–R star from Pérez-González et al. (2006). The presence of a cluster can be inferred in the HST image even in the three W–R locations without an association with a named complex. If the W–R location is part of the CSC or close to it, we list the name of the CSC from Santiago-Cortés et al. (2010) in column 9. Column 10 contains the distance of the W–R star from the nearest CSC. In five cases, the W–R star occupies the core of the compact cluster. Two of our W–R locations (WR3 and WR14) are part of a same complex, whereas one (WR6) is clearly outside a CSC, with the nearest CSC at a distance of about 90 pc. This is most likely a runaway W–R star, which are found at distances as far as 120 pc from the parent clusters (e.g. runaway O star in the dense LMC cluster R136 in 30 Dor complex; Evans et al. 2010).

The ionized gas has a symmetric bubble morphology in one case (WR7), whereas in rest of the cases, a shell-like structure extends on one side of the cluster. The sizes of the bubbles/shells range from ∼50–250 pc (see column 11).

2.6 Photometry of W–R objects

Having located the W–R objects on the *HST* images, we carried out aperture photometry of these objects using IRAF/phot. An aperture radius of 0.2 arcsec was used, and an aperture correction factor for an infinite aperture was applied, along with their zeropoints (*F*435*W*: 0.03, 25.579; *F*606*W*: 0.03, 25.00; *F*814*W*: 0.03, 25.501).

A colour–magnitude diagram using these data is shown in Fig. 4, where we compare their positions with evolutionary tracks for massive stars at solar metallicity from Geneva models (Ekström et al. 2012, standard mass-loss and no rotation). The plotted models indicate that the magnitudes and colours of our objects are consistent with them being individual stars. The evolutionary tracks indicate masses of our W–R stars between ∼11 and 120 $M_\odot$. However, in these models W–R properties (hydrogen abundance <40 per cent and $T_{\rm eff}$ > 10000 K) are generated only for masses >32 $M_\odot$. Inclusion of rotation in models, or binarity can resolve this apparent problem regarding the minimum mass that goes through the W–R phase. The observed range of magnitudes and colours are in the range of the values for individual W–R stars in the MW (see table 2 in Crowther 2007, and references therein).

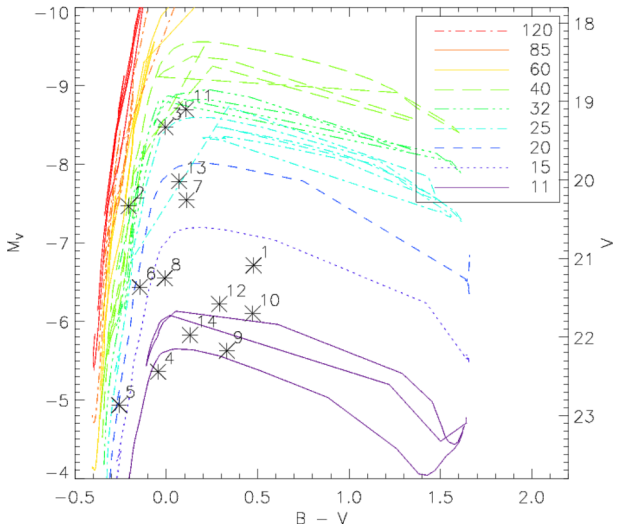

Figure 4. Colour–magnitude diagram (CMD) for the 14 W–R stars in M81 (asterix), each identified by its number. The left axis shows the absolute magnitude, whereas the right axis shows the observed magnitude, both in the *HST F*606*W* (*V*) band. Evolutionary tracks at solar metallicity from Geneva models (Ekström et al. 2012, standard mass-loss and no rotation) are shown for masses between 11 (bottom most) and 120 $M_\odot$ (top most), indicated with different line types and colours at the top-right corner.

3 ANALYSIS OF W–R FEATURES

The blue and red bumps of the W–R stars are made up of several broad emission lines. It is customary to relate the blue bump to WN subtype, being dominated by the He II λ4686 and N III λλ4634/42, whereas the red bump is associated with the C IV λλ5802/12 line from the WC subtype. The blue bump has a contribution from C III λ4650/C IV λ4658 line as well. Additionally, nebular lines of He II λ4686, He I λ4713, [N II] λ5755 and He I λ5876 can be present superposed on the broad bumps.

WN and WC stars are further classified into subtypes WN2–9 and WC4–11 (Smith 1968; Smith, Shara & Moffat 1996; Crowther, De Marco & Barlow 1998). WN2–5 and WC4–6 are known as early (WNE and WCE), with the higher numbered subclasses referred to as late (WNL and WCL) types. Early types show lines of higher ionization state (N IV, N V in WNEs; C IV in WCEs) as compared to the late types (N III in WNL; C III in WCL). Smith, Crowther & Prinja (1994) has extended the WN classification in order to include Of stars. These stars are given types WN10–WN11. Often, these stars show hydrogen lines in emission and/or absorption.

For an accurate classification of subtypes in each of WN and WC classes, it is important to determine the strength of the diagnostic lines without contamination from other lines. Often the quality of the available spectra does not permit identification of all diagnostic lines. In such cases, subtypes have been determined by making use of templates either obtained observationally (e.g. Crowther & Hadfield 2006) or theoretically (e.g. Hamann & Gräfener 2004).

The nebular-subtracted spectra are analysed using template spectra of individual W–R stars in order to determine (1) the number of W–R stars responsible for the observed strength of W–R features, and/or (2) the W–R subtype(s) of the contributing star(s). We used the observed templates of LMC stars,[7] that are kindly provided to

[7] The metallicity of the observed regions in M81 resembles that of the Milky Way. However, as of now templates are available only for LMC and SMC W–R subtypes.

Table 3. Classification of the W–R stars of our sample.

ID (1)	f_{WNL} (2)	f_{WNE} (3)	f_{WCE} (4)	Class (5)
WR1	–	–	0.5	1WCE
WR2	–	–	1.0	1WCE
WR3	1.9	–	1.5	2WNL+1WCE
WR4	–	1.4	–	1WNE
WR5	1.1	–	0.1	1WNE/CE
WR6	0.9	–	0.6	1WNL+1WCE
WR7	0.5	–	–	1WNL
WR8	–	0.4	–	1WNE
WR9	0.3	–	0.3	1WNL/CE
WR10	0.2	–	0.2	1WNL/CE
WR11	1.0	–	–	1WNL
WR12	–	0.7	–	1WNE
WR13	1.2	–	–	1WNL
WR14	0.4	–	0.1	1WNL/CE

Note. (1) W–R identification number; (2) factor by which WNL template has been multiplied to reproduce the observed features; (3) factor by which WNE template has been multiplied to reproduce the observed features; (4) factor by which WCE template has been multiplied to reproduce the observed features; (5) W–R classification of each star.

us by Paul Crowther (Crowther & Hadfield 2006). The template spectra were converted from luminosity to flux units by using the distance of M81. The resulting continuum level was found to be in general higher and bluer than the observed continuum of M81 W–R spectra. We hence added a power-law continuum to the template so as to reproduce the observed continuum. For our spectra containing a red bump (eight cases), we used the WC template and scaled it by a factor f_{WC} so as to match the observed strength of the red bump. In two cases, we found the scaled template also reproduced very well the observed strengths of the blue bump. These are pure WCE stars. In the remaining six cases, we found that there is a systematic residual on the blue edge of the observed blue bump. In these cases, we added a WNL or WNE template spectrum and scaled it by another factor f_{WN} so as to reproduce the observed blue bump strength. In rest of the cases with only a blue bump, a scaled WN template is found to reproduce the observed bump profiles very well. Results of the classification are summarized in Table 3.

The best-fitting combination of template spectra is shown superposed on the nebular-free observed spectra in Fig. 5. The spectra are organized in four panels, with the first two corresponding to WNLs and WNEs, respectively, the next one containing WCEs in single and multiple stars. The last panel shows the cases that require both WN and WC with $f_{WN}+f_{WC}\lesssim 1$.

The scaling factor between the template and the observed bump strengths is an indicator of the number of W–R stars that are required to produce the observed strength of the bumps in our spectra. The values of f_{WN} and f_{WC} lie in the range of 0.3–1.7, and 0.5–1.5, respectively. These values indicate that our spectra, though passing the cluster centres, require at the most a couple of W–R stars. The derived non-integer scaling factor is not unexpected, given the large dispersion in the strength of W–R features in the spectra used to obtain the template spectra.

Crowther & Hadfield (2006) find that the strength of the red bump varies by 48 per cent in different WCE stars, whereas the blue bump strength varies by as much as 60 per cent and 71 per cent in WNLs and WNEs, respectively. Thus, the scaling factor for a single WCE star could lie anywhere between 0.5 and 1.5, for a single WNL star between 0.4 and 1.6, and for a single WNE star between 0.3 and 1.7. We used this criterion to determine the number of WNL, WNE and WCE stars contributing to a spectrum.

Before we go ahead determining the number of W–R stars contributing to each spectrum, we discuss the effect of metallicity differences between the template and our spectra. Metallicity of ionized nebulae in M81 has been studied in detail by Arellano-Córdova et al. (2016), who found a mean value of $12+\log(\frac{O}{H}) = 8.58 \pm 0.06$ with a gradient as small as 0.01 dex kpc^{-1}. The templates used for fitting correspond to that of the LMC, which has a metallicity around a third of the values for our regions. According to Crowther & Hadfield (2006), the W–R spectrum at higher metallicities is expected to be similar to that of the LMC template used in our work, with the strength of the bumps increasing with increasing metallicities. Thus, the bumps in M81 spectra are expected to be marginally stronger than those in the template spectra. As a consequence, single star f_{WC} and f_{WN} values could be marginally higher than 1 for the W–R stars in M81.

Among the eight cases where we required only one template, three are WNLs ($f_{WN} = 0.5$, 1.0 and 1.2), three WNEs ($f_{WN} = 0.4$, 0.7 and 1.4) and two WCEs ($f_{WC} = 0.5$ and 1.0). Using the criteria discussed above for quantification of number of W–R stars, the derived scaling factors suggest 1 star in all these cases, even after taking into consideration differences in metallicity between the template and M81. Among the remaining six spectra, WR3 and WR6 are multiple systems requiring at least three and two W–Rs, respectively, of at least one WNL and WCE sub-types. The remaining four stars have f_{WC} values less than the minimum expected for a single WCE star. In fact the sum of $f_{WC}+f_{WN}$ (0.4, 0.45, 0.6 and 1.18) suggests a single star. All these spectra have strong red bump, indicating the presence of a WC component, and the blue bump clearly contains the N III line, the characteristic signature of a WN component. Do these four cases represent multiple systems containing sub-luminous W–R stars? As discussed above, the metallicity difference between the template and M81, if at all, is expected to increase the strengths of the bumps, and hence systematically sub-luminous W–R stars are not expected due to metallicity differences. However, there exist sub-luminous WN stars such as WR24, a WN6ha star in the Milky Way, whose bump strength is an order of magnitude lower as compared to other stars of the same sub-type (Crowther 2007). These are extreme cases, and hence it is statistically improbable that four of our objects contain multiple stars of extreme WN and WC types.

Are these four objects transitional W–R stars? Conti & Massey (1989) defined a sample of 8 Galactic W–R stars that have prominent spectral lines corresponding to both WN and WC stars, which they called as transitional objects (WN/Cs). Stellar evolutionary tracks of Geneva (Meynet & Maeder 2003) with rotation produce these stars as those stars evolving from WN to WC subtype, with this transitional phase lasting for ∼4 per cent of the W–R lifetime. Thus, they are expected to comprise only ∼4 per cent of our sample. In fact, the first transitional object in M31 is reported only recently after the discovery of more than 150 W–R stars (Shara et al. 2016). In this context, it is extremely rare to have 4 transitional types in our sample of 14 W–Rs. In the next section, we discuss the photometric and spectroscopic properties of these stars in order to find out whether they could be two independent stars within our slit or they are most likely to be transitional objects.

4 DISCUSSION

Two of our 14 W–R locations require multiple W–R stars. Among the remaining 12, eight are clear cases of single stars (3 WNLs,

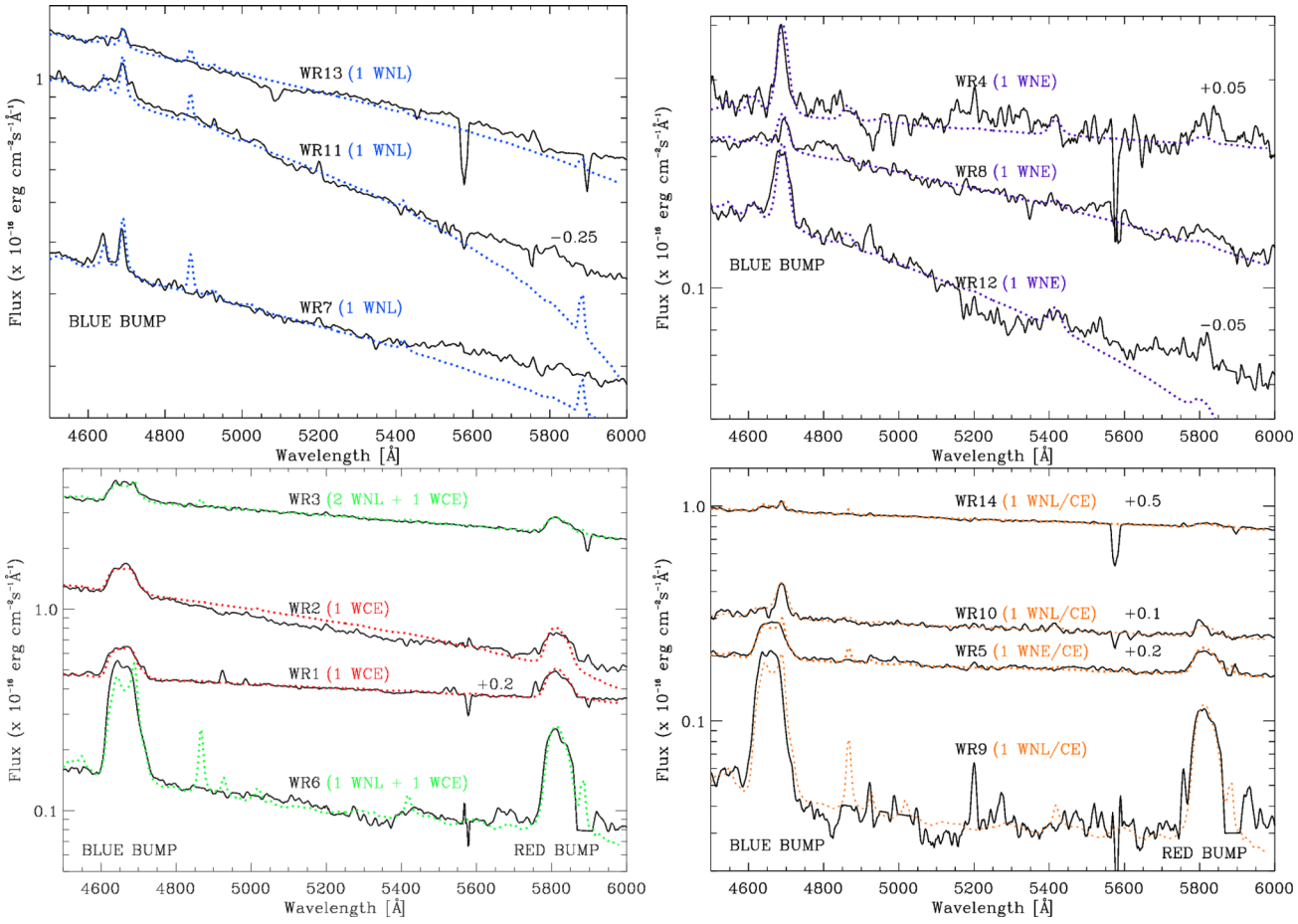

Figure 5. Observed nebular-free spectrum (solid line) is shown along with the best-fitting template W–R spectrum (colour dotted line). The estimated number of W–R stars is indicated in parenthesis. To avoid overlap, spectra are shifted by the indicated amount (−0.25 dex, +0.05 dex etc.) in a few cases. The top two panels contain WNL and WNE stars. Spectra of our locations containing at least one WCE star are shown in the bottom-left panel, and the transitional WN/C stars are shown the bottom-right panel.

3 WNEs and 2 WCEs). The remaining four cases require features from both WN and WC templates, but not strong enough to suggest two independent WN and WC stars. We now analyse all our stars in diagrams involving the line strengths, magnitudes and FWHM. In particular, we investigate whether the four stars that require both WN and WC templates could be of transitional type, classified as WN/C type, could have contribution from two or more stars, at least one each being WN and WC.

W–R bumps have asymmetric form, with contributions from multiple lines. Multiple Gaussian fitting has been used by Brinchmann, Kunth & Durret (2008) with considerable success to obtain line strengths of individual components. We here intend to obtain the total strength of the bumps, and hence used simple numerical integration (the command stroke *e* of IRAF/*splot*) covering the blue and red bumps. When the red bump is not detected we determined an upper limit by calculating the 3σ fluxes over a width of 80 Å. We also measured the width of the blue and red bumps. The red bump is seen as a single broad line, to which we fitted a Gaussian profile to determine the FWHM. On the other hand, sub-structures are seen in all of our blue bumps. We fitted the Gaussian profile to the brightest of these sub-structures, which in most cases coincided with the rest wavelength of He II λ4686, to obtain the FWHM of the blue bump.

In Fig. 6, we plot the luminosity of the red bump against that of the blue bump. Different W–R subtypes are shown by different

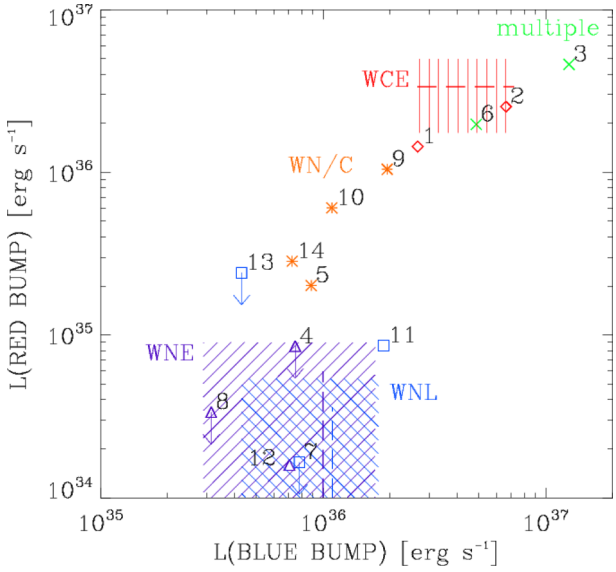

Figure 6. The luminosity of the red bump against that of the blue bump for our sample of W–R objects. Stars of same subtype are shown by a common symbol and colour. 3σ upper limits are shown when the red bump is not detected. The hatched areas show the values expected for the WNL, WNE and WCE templates of single stars.

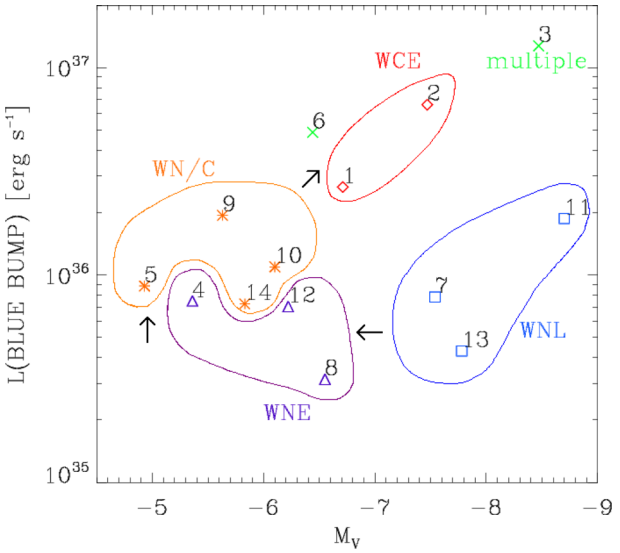

Figure 7. The blue bump luminosity of our W–R stars against the magnitude of the star in the *HST* image with which we associate the observed features. Stars of the same subtype are enclosed in contours. Arrows indicate the currently accepted evolutionary scenario in which massive O stars first appear as W–R stars of subtype WNL, going through WNE, and transitional WN/C phase before reaching the WC type.

symbols. The typical values of the bump strength as well as the dispersion over these values for WNL, WNE and WCE stars are also indicated. The plotted ranges for the blue bump in WN and WC stars, and the red bump in WC stars are based on the values in table 1 and table 2 of Crowther & Hadfield (2006). Considering that a range of the red bump strength (or an upper limit) in WN stars is not given in these tables, we used the WN template spectra to measure their strength. In order to plot an upper limit, we assumed a dispersion of 50 per cent over the measured values, which are in the same range as the values tabulated by Crowther & Hadfield (2006).

As expected, the classified WNL, WNE and WCE stars have both their blue and red bump luminosities within the range of values for the corresponding sub-types. W–R locations with multiple W–Rs (WR3 and WR6) occupy a zone in the range for WCE stars or above it. These systems contain at least one WCE star, which have both their bumps much brighter than those in WN stars, and hence dominate the combined luminosities. On the other hand, for the transitional types, the observed blue bump luminosities are in the range expected for WN stars, but they have clearly excess red bump luminosities compared to that of WN stars. At the same time, the observed red bump luminosities are lower than the values expected for the WC type. Moreover, the transitional stars follow a diagonal line where the red bump luminosity increases proportionately with the blue bump luminosity. It is hard to imagine a combination of multiple W–R stars of WN and WC types contriving to produce the observed trend. Any such combination would require WC stars that are underluminous by as much as by a factor of 10 in their red bump strength.

We now plot in Fig. 7 the blue bump luminosity of our W–R stars against the magnitude of the star in the *HST* image with which we associate the observed features. Same symbols as in the previous figure have been retained. All stars of a given sub-type group together, which are shown by roughly drawing contours enclosing the stars of that sub-type. The WNL sub-type, which is the earliest stage of a W–R phase, occupies the right-bottom part. The WNE stars, which are the descendants of WNL stars, occupy the left-

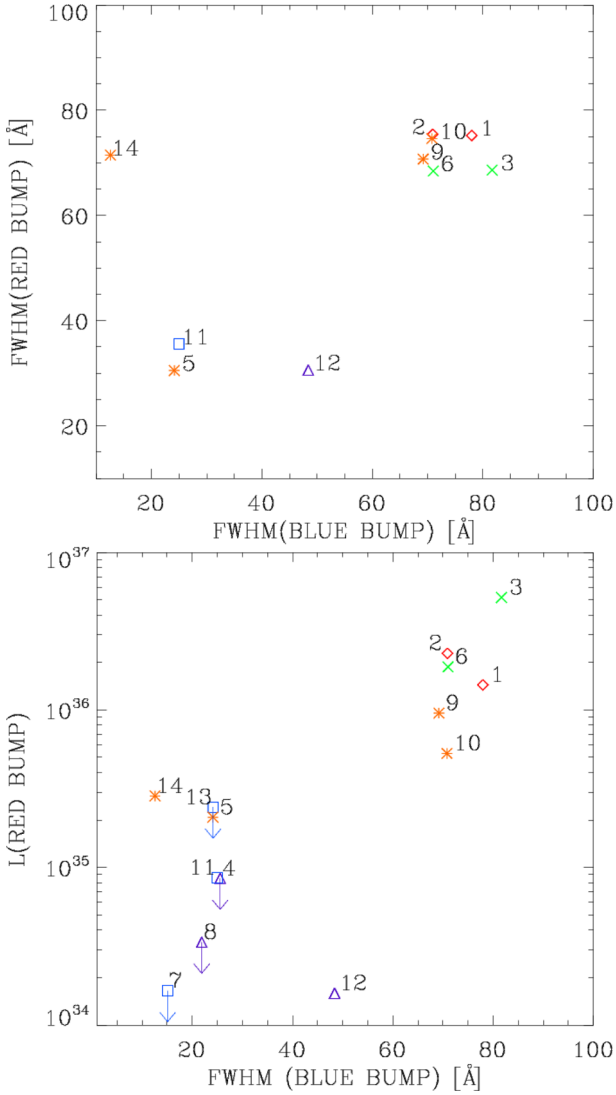

Figure 8. The FWHM of the red bump against the FWHM of the blue bump (top) and red bump luminosity against the FWHM of the blue bump (bottom).

bottom part. On the other hand, the WCE stars, which denote the last phase of a W–R star, occupy the upper part of the diagram. We have indicated by arrows this evolutionary scenario, first proposed by Conti (1976). Modern stellar evolutionary models (Meynet & Maeder 2003) reproduce the observed properties of W–R stars through the Conti scenario. These models, in addition, were able to reproduce the WN/C stars as those undergoing transition from WNE to WC phase. In our figure, these WN/C stars occupy a region between WNE and WC stars, further illustrating that these stars are transitional stars rather than multiple systems, which occupy the top-most part of our diagram. It may be noted that our WN/C stars are among the faintest in our sample again hinting that it is unlikely that it is a multiple system of stars.

One of the characteristic signatures of a WC star is its broad bumps with the red bump having FWHMs >50 Å (see e.g. fig. 4 in Crowther & Hadfield 2006). In Fig. 8, we show the FWHM of the red bump against the FWHM of the blue bump. As expected, WCE stars occupy the top-right corner of the plot having values between 70 < FWHM < 100 Å. Two of our transitional stars, and multiple systems, also occupy this corner. One of the transitional

stars (WR5) has FWHM < 30 Å for both the bumps. This latter value is the typical value of FWHM in WNs (see e.g. fig. 2 in Crowther & Hadfield 2006). We illustrate this in the bottom panel by plotting the observed strength of the red bump (or an upper limit when the red bump is not detected) against the FWHM of the blue bump. It is interesting to note that there is only one object (WR12) with measured FWHM between 30 and 70 Å. In the transitional object WR5, both blue and red bumps have their FWHM of a WN star. On the other hand, in WR14, another transitional object, the red bump is as broad as that of WCs, and the blue bump has FWHM typical of WNs. The other two transitional stars have both their bumps broad like in WCs. Hence, mixed properties of WR5, WR9, WR10 and WR14 suggest that they are more likely to be transitional objects of type WN/C rather than multiple system containing a WN and a WC star.

5 CONCLUSIONS

In this work, we reported the discovery of 14 locations in M81 where we found spectral signatures for the presence of W–R stars. All the locations were serendipitously discovered along the GTC long-slit and MOS spectra of targeted compact stellar clusters. At each location, we identified a candidate object in the *HST* image that is responsible for the W–R features. We analysed our W–R spectra using template spectra of WN and WC stars to obtain the number and sub-type of W–R star(s) that are responsible for the strength of the observed features. We find clear case for multiple W–R stars in two locations, with the remaining 12 locations requiring only one W–R star. We classify three of them as WNLs, three as WNEs, and two as WCEs. Four stars are found to have their red bumps too strong to be of WN type, but not strong enough to be of WC star. All the observed properties of these four stars are consistent with them being transitional WN/C stars. However, 4 out of our sample of 14 is statistically high as compared to the 4 per cent expected in stellar evolutionary models. A narrow-band imaging survey to detect W–R bumps of the whole galaxy would be required to address the reason for the observed abnormally high fraction of transitional stars in our serendipitous sample.

ACKNOWLEDGEMENTS

It is a pleasure to thank Antonio Cabrera and the rest of the GTC staff for their help in carrying out the observations presented in this work and also for the support during data reductions. We thank the Hubble Heritage Team at the Space Telescope Science Institute for making the M81 images publicly available. This work is partly supported by CONACyT (Mexico) research grants CB-2010-01-155142-G3 (PI:YDM) and CB-2011-01-167281-F3 (PI:DRG). VMAGG thanks CONACyT for the research scholar fellowship that is granted to him. The paper has gained enormously from the suggestions of a referee on an earlier version.

REFERENCES

Arellano-Córdova K. Z., Rodríguez M., Mayya Y. D., Rosa-González D., 2016, MNRAS, 455, 2627
Bibby J. L., Crowther P. A., 2010, MNRAS, 405, 2737
Breysacher J., Azzopardi M., Testor G., 1999, A&AS, 137, 117
Brinchmann J., Kunth D., Durret F., 2008, A&A, 485, 657
Conti P. S., 1976, Proc. 20th Colloq. Int. Astrophys., Liege, p. 193
Conti P. S., Massey P., 1989, ApJ, 337, 251
Crowther P. A., 2007, ARA&A, 45, 177
Crowther P. A., Hadfield L. J., 2006, A&A, 449, 711
Crowther P. A., Hillier D. J., Smith L. J., 1995, A&A, 293, 172
Crowther P. A., De Marco O., Barlow M. J., 1998, MNRAS, 296, 367
Ekström S. et al., 2012, A&A, 537, 18
Evans C. J. et al., 2010, ApJ, 715, 74
Freedman W. L. et al., 1994, ApJ, 427, 628
Hadfield L. J., Crowther P. A., Schild H., Schmutz W., 2005, A&A, 439, 265
Hamann W. R., Gräfener G., 2005, A&A, 427, 697
Hillier D., 2000, Encyclopedia Astron. Astrophys., 1895
Kehrig C. et al., 2013, MNRAS, 432, 2731
Massey P., 2003, ARA&A, 41, 15
Mayya Y. D., Rosa-González D., Santiago-Cortés M., Arellano-Córdova K., Rodríguez M., 2013a, Rev. Mex. Astron. Astrofis. Ser. Conf., 42, 22
Mayya Y. D., Rosa-González D., Santiago-Cortés M., Rodríguez-Merino L. H., Vega O., Torres-Papaqui J. P., Bressan A., Carrasco L., 2013b, MNRAS, 436, 2763
Mayya Y. D., Santiago-Cortés M., Rosa-González D., Gómez-González M., Rodríguez L., Carrasco L., 2014, in Mayya Y. D., Rosa González D., Terlevich E.. eds, 2013 Guillermo Haro Conf., INAOE & AMC, Mexico City, p. 147
Meynet G., Maeder A., 2003, A&A, 404, 975
Meynet G., Maeder A., 2005, A&A, 429, 581
Miralles-Caballero D., Rosales-Ortega F. F., Díaz A. I., Otí-Floranes H., Pérez-Montero E., Sánchez S. F., 2014, MNRAS, 445, 3803
Neugent K. F., Massey P., 2011, ApJ, 733, 123
Neugent K. F., Massey P., Georgy C., 2012, ApJ, 759, 11
Patterson M. T., Walterbos R. A. M., Kennicutt R. C., Chiappini C., Thilker D. A., 2012, MNRAS, 422, 401
Pérez-González P. G. et al., 2006, ApJ, 648, 987
Santiago-Cortés M., Mayya Y. D., Rosa-González D., 2010, MNRAS, 405, 1293
Schaerer D., Vacca W. D., 1998, ApJ, 497, 618
Schlafly E. F., Finkbeiner D. P., 2011, ApJ, 737, 103
Shara M. M., Bibby J. L., Zurek D., Crowther P. A., Moffat A. F. J., Drissen L., 2013, ApJ, 146, 162
Shara M. M., Mikołajewska J., Caldwell N., Iłkiewicz K., Drozd K., Zurek D., 2016, MNRAS, 455, 3453
Smith L. F., 1968, MNRAS, 138, 109
Smith L. J., Crowther P. A., Prinja R. K., 1994, A&A, 281, 833
Smith L. F., Shara M. M., Moffat A. F. J., 1996, MNRAS, 281, 163
Terlevich E., Díaz A. I., Terlevich R., González-Delgado R. M., Pérez E., García Vargas M. L., 1996, MNRAS, 279, 1219
van der Hucht K. A., 2001, New Astron. Rev., 45, 135
Vanbeveren D., 2011, Proc. 39th Lige Astrophysical Colloq., 80, 530
Woosley S. E., Bloom M. J., 2006, ARA&A, 44, 507

This paper has been typeset from a TEX/LATEX file prepared by the author.